Chapter 6

Z-scheme $Ag_2MoO_4/CuWO_4$ photocatalysts for dye degradation

6.1. Introduction

Organic dyes are one of the most significant pollutants released into the environment by the textile, printing, food, leather, cosmetics, and pharmaceutical industries (Farhan Hanafi & Sapawe, 2020; Pavithra et al., 2019; Tkaczyk et al., 2020). They typically have complex aromatic molecular structures, which makes them more stable and difficult to biodegrade. These colored compounds reduce sunlight penetration into the stream, affecting the aquatic ecosystem. The leading impact of such dyes is the resulting high biochemical oxygen demand and toxicity (Morshed et al., 2020; Sargin et al., 2020; Zhang et al., 2021).

Antibiotic pharmaceuticals are another crucial class of organic pollutants. They are released into the environment by an animal or a human in a partially metabolized state (Gothwal & Shashidhar, 2015). The target bacteria and microorganisms become antibiotic-resistant as their environmental abundance increases (García et al., 2020; Kumar & Pal, 2018; Patel et al., 2019). Methods like adsorption, membrane separation, electrolysis, and photocatalysis have been used to remove drugs from natural water (Zhu et al., 2019). Heterogeneous photocatalysts can oxidize and degrade such pollutants in an economical and environmentally friendly method (Behera et al., 2021). Photocatalysis involves photoexcitation using light of a suitable wavelength. Electrons and holes, photoinduced charge carriers, are created in the conduction (CB) and valence band (VB), respectively. Photoexcited VB holes can oxidize species with a higher positive reduction potential. Similarly, the CB position with higher negative reduction potential determines the chance of a molecular species' photo-reduction. Reactive species on the photocatalytic surface like h^+, $O_2^{\bullet-}$, and $^{\bullet}OH$ radicals are responsible for the degradation of organic pollutants (Karthikeyan et al., 2020). However, a single-phase photocatalyst has issues with adsorption, limitations in VB/CB positions, and fast

recombination (Guo et al., 2018). A heterojunction-based photocatalyst can reduce recombination and induce better charge separation (Paramanik et al., 2018).

As mentioned in earlier Chapters, $CuWO_4$ is well-known n-type semiconductor having an indirect band gap ranging from 2.2 to 2.4eV and good stability against photo corrosion at neutral pH (Moura et al., 2020). Different morphologies of $CuWO_4$ have been used for applications such as water splitting, photocatalytic degradation of organic pollutants, gas sensing, etc (Raizada et al., 2020; Tian et al., 2019). Over the last decade, silver molybdate (Ag_2MoO_4) has received a great deal of attention in photoluminescence, biological sterilization, and electrocatalytic oxygen reduction reaction (Gouveia et al., 2022; Huo et al., 2018). It has also been demonstrated to be an excellent semiconductor for fabricating more effective heterojunction photocatalysts with other semiconductors suitably aligned bandgaps (Gouveia et al., 2022). Examples include composite photocatalysts like $Ag/AgCl/Ag_2MoO_4$ (Jiao et al., 2019), and $Ag@Ag_2MoO_4$-AgBr (Bai et al., 2016), β-$Ag_2MoO_4/BiVO_4$ (Chen et al., 2019), Ag_2MoO_4/WO_3 (Wang et al., 2019), Ag_2MoO_4/Ag_3PO_4 (Cao et al., 2017). The band edges of Ag_2MoO_4 are staggered concerning those of $CuWO_4$. Based on the above literature, $Ag_2MoO_4/CuWO_4$ heterojunction photocatalyst is new and should perform well.

This study used a stepwise hydrothermal precipitation process to prepare heterojunction $Ag_2MoO_4/CuWO_4$ photocatalysts for RhB degradation. The percentage of Ag_2MoO_4 loading on $CuWO_4$ was varied, affecting the photocatalytic activity. These heterojunction photocatalysts' photocatalytic actions were compared to those of pure $CuWO_4$ and Ag_2MoO_4 materials. The photocatalysts were characterized by X-ray diffraction (XRD), transmission electron microscopy (TEM), X-ray photoelectron spectroscopy (XPS), and Ultraviolet-visible diffuse reflectance spectroscopy (UV-Vis DRS). Photoluminescence spectroscopy was used to examine the migration of carriers

and the proportional recombination of photoinduced charge carriers. Aspects of the RhB photocatalytic degradation mechanism were investigated through trapping experiments.

6.2. Experimental details

6.2.1. Synthesis of $Ag_2MoO_4/CuWO_4$

The following steps were used to prepare the $Ag_2MoO_4/CuWO_4$ nanocomposite. One millimole of as-prepared $CuWO_4$ nanoparticles was dispersed in 15 mL DI (deionized) water and sonicated for 30 minutes. Next, 0.05 mmol in 20 mL of $AgNO_3$ was added dropwise into the re-dispersed $CuWO_4$ suspension. The suspension was magnetically stirred in the dark for about 30 min and then put on a thermostatic shaker for 24 hours. The latter was to ensure the complete adsorption of Ag^+ ions on the surface of $CuWO_4$. The next step was the dropwise addition of 20 ml of (0.025 mmol) $Na_2MoO_4 \cdot 2H_2O$ solution under continuous agitation to the previously prepared mixture. A precipitate of the composite product was formed. All the experimental procedures were carried out in complete darkness to prevent Ag formation. The same procedure was used to create $Ag_2MoO_4/CuWO_4$ photocatalysts in various concentrations. The weight percentages of Ag_2MoO_4 in the three composites prepared were 5%, 10%, and 15%, respectively. These composite samples are designated by the 5% MW,10% MW, and 15% MW labels.

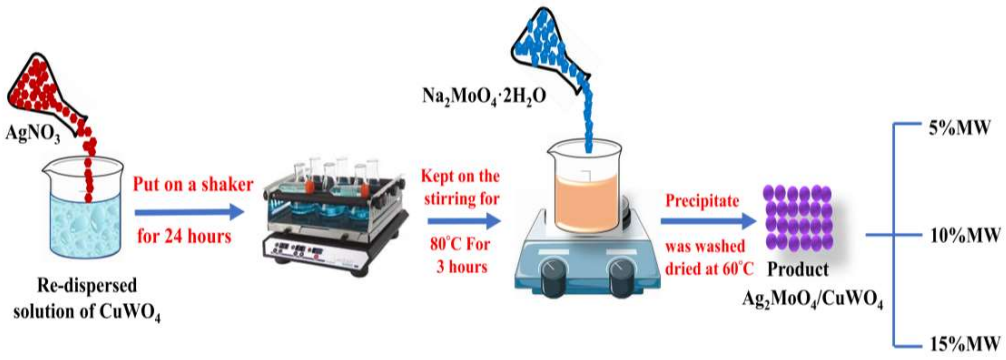

Scheme 6.1. A schematic of the preparation procedure of $Ag_2MoO_4/CuWO_4$ composites

6.2.2. Photocatalysis experiments

$Ag_2MoO_4/CuWO_4$ composite capabilities for RhB degradation under ultraviolet irradiation have been assessed. A high-pressure mercury lamp of 250W served as a light source. In a cuvette with a 1 cm path length, the reaction was conducted. The photocatalyst (2 mg/4 ml) dispersion was added in 200 µl of 20 ppm solutions of RhB at optimum pH. For one hour, the produced mixtures were agitated in the dark to promote adsorption-desorption equilibrium. In this process ~5% of RhB is adsorbed on catalyst surface. Each reaction mixture was then placed beneath a source of UV light. UV visible spectrophotometry was used to track the breakdown of the targeted organic pollutants at regular intervals.

$$\text{Removal Efficiency} = \left(\frac{C_o - C_t}{C_o}\right)x100 \qquad \text{---------- (6.1)}$$

In equation (6.1), the notation C_0 represents the initial concentration, and C_t is the final concentration.

6.3. Results and Discussion

6.3.1. XRD analysis

The XRD patterns of $CuWO_4$, Ag_2MoO_4, and their composites are shown in Fig. 2. Intense peaks at 2ɵ values of 19°, 22.9°, 23.5°, 24.1°, 25.9°, 26.9°, 28.7°, 30.8°, 31.6°, 32.1°, 34.4°, and 38.6° are particularly prominent in the XRD of pure $CuWO_4$. These are indexed to the crystal planes (001), (100), (110), (0 1 1), (0 1 1), (011), (1 01), (101), (1 01), (1 1 1), (111), (020), (1 11), (1 1 1), (120), and (200) of the $CuWO_4$ triclinic structure (JCPDS File No. 72-0616), respectively (Tian et al., 2019). The characteristic diffraction peaks observed in the XRD for the prepared sample of Ag_2MoO_4 were at 27.1°, 31.8°, 33.3°, 38.6°, 50.9° and 55.8° (Sousa et al., 2020). These correspond to the planes (220), (311), (222), (400), (511), and (440) of the body-centered cubic structure of Ag_2MoO_4 (JCPDS File No. 08-0473)). The XRDs of the nanocomposite samples

(5% MW, 10% MW, and 15% MW) exhibit peaks corresponding to the triclinic $CuWO_4$ and the bcc Ag_2MoO_4 crystal structures.

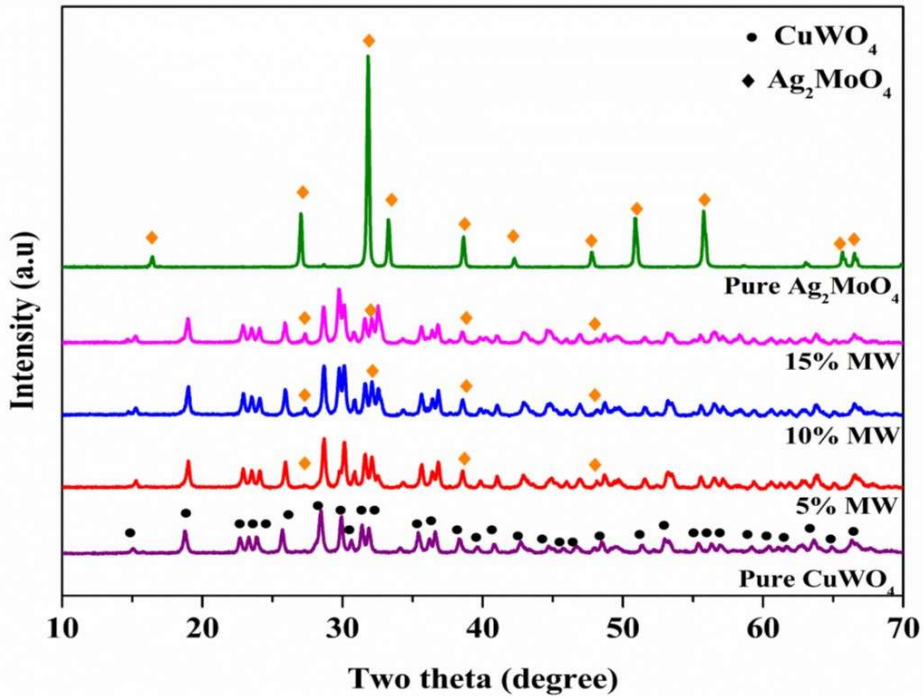

Fig. 6.1: Powder XRD diffraction patterns of the prepared materials pure $CuWO_4$, pure Ag_2MoO_4, 5% MW, 10% MW, and 15% MW

6.3.2. Morphology and heterostructures interface analysis

The TEM images of pure $CuWO_4$, 5% MW, 10% MW, and 15% MW are shown in Fig. 6.2. Pentagonal and hexagonal structures can be seen in the as-prepared $CuWO_4$ nanostructures. Plenty of tiny particles of Ag_2MoO_4 are homogeneously distributed on the surface of $CuWO_4$ nanostructures (Fig. 6.2 b-d). Fig. 6.3 depicts the HR-TEM images of the 10% MW sample since it has higher photocatalytic activity than other materials in this investigation. The lattice spacing of 0.331 nm in the HRTEM image of the 10% MW nanocomposite is assigned to the (110) plane of pure $CuWO_4$. Another lattice spacing of 0.233 nm corresponds to the (400) plane of bcc Ag_2MoO_4 (Fig. 6.3). The adjacent locations of these two lattice fringes in the HRTEM image of the composite confirm the formation of the $Ag_2MoO_4/CuWO_4$ composite.

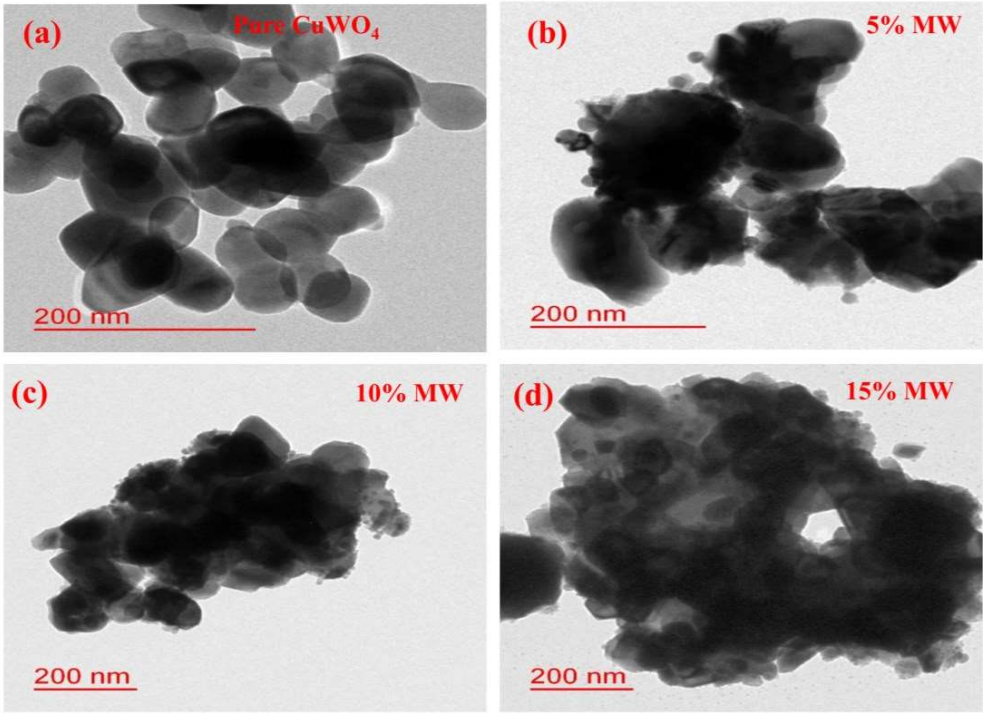

Fig. 6.2: TEM images of pure (a) $CuWO_4$, (b) 5% MW, (c)10% MW, and (d)15% MW

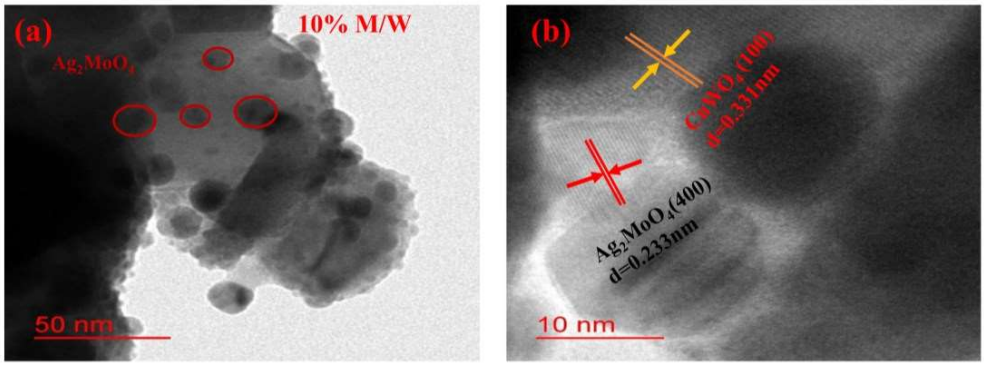

Fig. 6.3: HR-TEM images of 10% MW nanostructure showing fringes

6.3.3. XPS analysis

Peaks of Cu, W, O, Ag, and Mo can be seen in the survey spectrum of the 10% MW sample. The C1s peak, which has a binding energy (BE) of 284.8 eV, was used as the reference point. Fig. 6.4 compares the high-resolution (HR) spectra of Cu and W in 10% MW and $CuWO_4$ samples. The $Cu2p_{3/2}$ and $Cu2p_{1/2}$ peaks are observed at 933.5 and 953.1 eV in the Cu2p HR spectrum of the $CuWO_4$ (Fig. 6.4a) sample. These peaks

move to 933.8 and 953.6 eV in the 10% MW HR spectrum. The W4f (+6 oxidation state of W) area (Fig. 6.4b) has two peaks at 34.8 and 37.1 eV. These peaks can be seen in the 10% MW spectrum at 35.2 and 37.3 eV, respectively. The high-resolution spectrum of the Ag 3d region, corresponding to the binding energies of $Ag3d_{5/2}$ and $Ag3d_{3/2}$, shows two typical peaks for both pure Ag_2MoO_4 and the 10% MW samples. These peaks appear at 367.4 and 373.1 eV in the Ag_2MoO_4 spectrum. The peaks shift to 367.1 eV and 373 eV (Fig. 6d) in the 10% MW XPS. However, compared to the pure Ag_2MoO_4, the composite's two Mo3d peaks (Fig. 6.4e) are at slightly lower binding energies at 231.3/231.1($3d_{5/2}$) eV and 234.6/234.1 ($3d_{3/2}$) eV respectively. The O1s peak of $CuWO_4$ is at 530.2 eV (Fig. 6.4c). In contrast, the O1s peaks of Ag_2MoO_4 could be deconvoluted to peaks at 530.2 and 531.3 eV values. These peaks appear at 530.2 eV and 531.2 eV, respectively, in the 10% MW spectra. One cannot attribute the observed shift to a particular component because oxygen is present in the $CuWO_4$ and Ag_2MoO_4 components of the composite. The values of the Cu and W BEs in 10% MW are higher than those seen in the pure $CuWO_4$ spectrum. The values of the BEs for Ag and Mo in the 10% MW spectrum are somewhat lower than those seen for pure Ag_2MoO_4. The transport of electrons from $CuWO_4$ to Ag_2MoO_4 in the composite is the cause of the positively shifted $CuWO_4$ BEs and negatively shifted Ag_2MoO_4 peaks (Cao et al., 2017). Therefore, photoexcitation causes the migration of electrons from $CuWO_4$ to Ag_2MoO_4.

The valence band XPS spectra of $CuWO_4$ and Ag_2MoO_4 are shown in Fig. 6.5a and Fig. 6.5b. The intersection of the fits to the two linear parts of this curve was used to determine the VB maximum point. $CuWO_4$ and Ag_2MoO_4 have VBs at 1.56 eV and 1.44 eV, respectively.

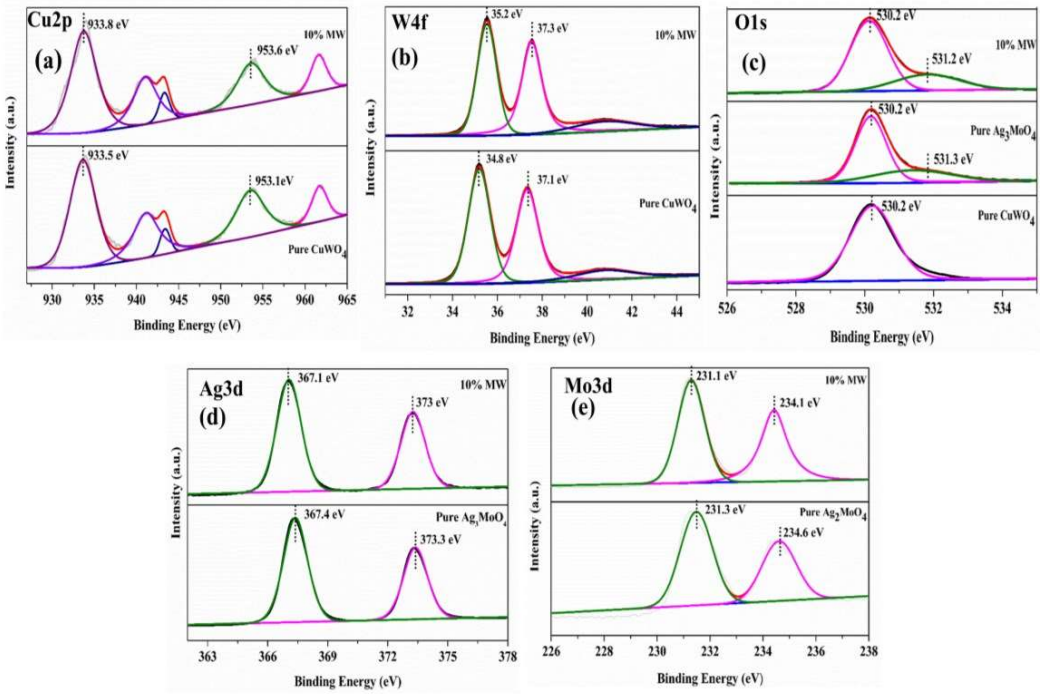

Fig. 6.4: Comparison between HR-XPS spectrums of different regions of 10 % MW with the spectrums of Ag_2MoO_4 and $CuWO_4$, (a) Cu2p, (b) W1s, (c) O 1s, (d) Ag 2p, and (e) Mo3d.

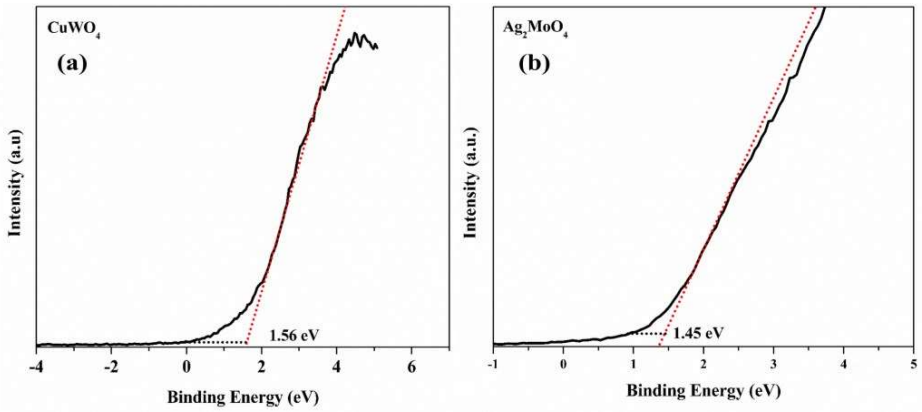

Fig. 6.5: The valence band XPS spectra of (a) $CuWO_4$ and (b) Ag_3VO_4

6.3.4. Solid-state UV-visible spectroscopy

Fig. 6.6(a) illustrates the solid-state UV-visible absorption spectra of the prepared catalysts. The Tauc plots of the pure $CuWO_4$ and Ag_2MoO_4 phases are shown in Fig. 6.6(b). The band gaps of these two semiconductors were calculated by the following formula (Eq. 6.2).

$$(\alpha h\upsilon)^{1/n} = h\upsilon - E_g \qquad (6.2)$$

In equation (6.2), h stands for Planck's constant, υ is the frequency, Eg is the bandgap energy, and α is the molar absorptivity coefficient. For a direct transition, the exponent n is 2, whereas, for an indirect transition, it's 1/2. The bandgaps of these phases were determined using the x-axis intercept of the fit to the linear component of the Tauc plots (Cao et al., 2017). Pure $CuWO_4$ and Ag_2MoO_4 have indirect bandgaps of 2.4 eV and 3.3 eV, respectively. Additionally, $CuWO_4$ and Ag_2MoO_4 CB locations were established using Eq. 6.3.

$$E_{CB} = E_{VB} - Eg \qquad (6.3)$$

The calculated CB positions of $CuWO_4$ and Ag_2MoO_4 are -0.74 and -1.85 eV, respectively.

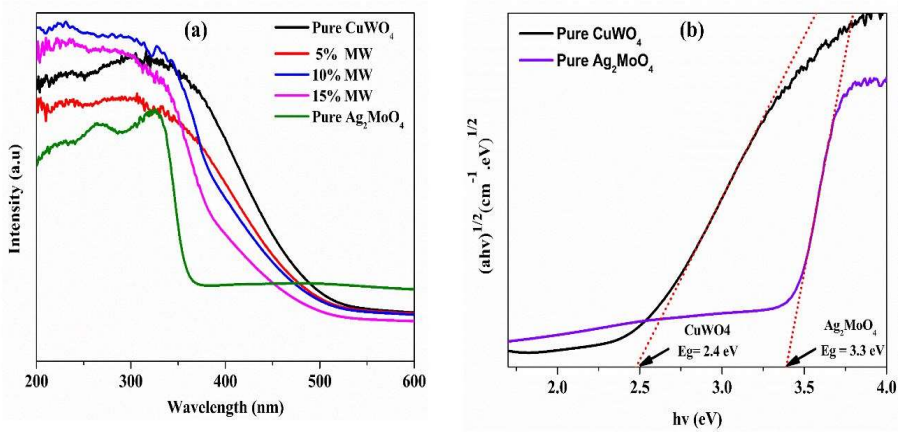

Fig. 6.6: (a) The solid-state UV − vis absorption spectrum of the nanomaterials prepared in this study. The $(\alpha h\nu)^{1/2}$ vs. energy hν Tauc plots and bandgap energy of the pure (b) $CuWO_4$ and Ag_2MoO_4 nanoparticles

6.3.5. Photoluminescence spectroscopy

The samples' relative photo-excited electron-hole recombination efficiency was determined by photoluminescence analysis (De et al., 2020; Jatav et al., 2021). The composites' excitation wavelength was 269 nm. Fig. 6.7 displays the photoluminescence spectra of the composite samples with various Ag_2MoO_4 loadings

on the $CuWO_4$ surface. Ag_2MoO_4 precipitating on $CuWO_4$ causes a reduction in fluorescence peak intensity. As a result, charge separation is improved, and the interfacial contact between Ag_2MoO_4 and $CuWO_4$ decreases the rate at which photoinduced charge carriers recombine. The fluorescence spectra of the 10% MW sample have the lowest intensity, showing that this is the ideal $Ag_2MoO_4/CuWO_4$ composition, according to the fluorescence spectrum. Excess loading of Ag_2MoO_4 in the composite prevents photoexcitation of the $CuWO_4$ surface.

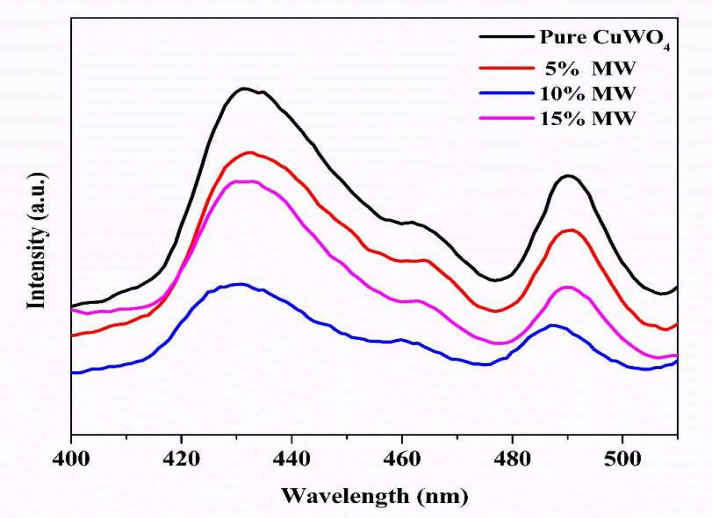

Fig. 6.7: Photoluminescence spectra of the prepared samples pure $CuWO_4$, 5% MW, 10% MW, and 15% MW

6.3.6. Evaluation of the photocatalytic activity

The degradation plots of RhB over the examined photocatalysts are displayed in Fig. 6.8. $CuWO_4$ nanoparticles barely degrade during RhB. Over Ag_2MoO_4 nanostructures, some RhB degradation does occur, albeit slowly. In contrast, the rate of degradation over 5% MW has slightly increased. The former is noticeably better when comparing RhB photocatalytic degradation to 10% MW and 15% MW samples. The 10% MW sample shows the best photocatalytic activity for RhB. Ag_2MoO_4 deposits on $CuWO_4$ result in charge separation and improved driving forces for reduction and oxidation.

But it also obstructs the illumination of $CuWO_4$. As a result of these conflicting elements, 10% MW composite exhibits better photocatalytic activity.

The degradation of Rhodamine B on a visible light photocatalyst generally involves a blue shift. The shift is primarily due to the transformation of the RhB molecules that have not been photocatalytically degraded. The RhB molecules get transformed by a de-ethylation reaction during photocatalysis (Yang &Yang, 2018). Rhodamine B is a dye with a maximum absorption peak (λ_{max}) at 554 nm. Hence, RhB also gets photo-excited when exposed to visible light irradiation. Jakimińska et. al., 2022 has investigated this issue and concluded that the N-de-ethylation process was primarily due to photo-excited electron transfer from the RhB molecule to the photocatalyst. Nevertheless, such a photosensitizer role of RhB is impossible when a UV light source is used because RhB does not absorb UV light and does not get photo-excited. Thus, no shift in RhB λ_{max} was observed when exposed to a UV light photocatalysis process.

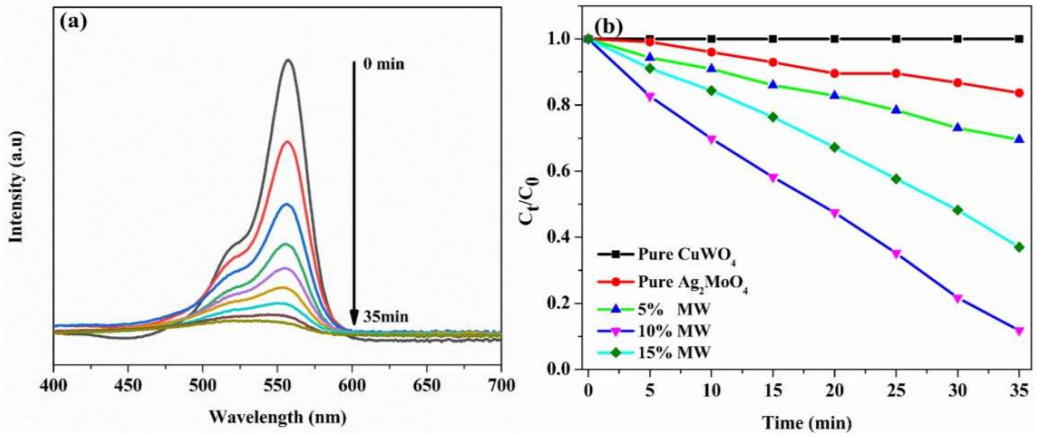

Fig. 6.8: Change in normalized RhB concentration with visible light exposure time on Pure $CuWO_4$, Ag_2MoO_4, 5% MW, 10% MW, and 15% MW in this study

The nanocomposite 10% MW created for this study's RhB degradation followed zero-order kinetics and its details have been given in Table 6.1 (Fig. 6.9).

Table 6.1: Rate constant (k) and correlation coefficient (R^2) for RhB degradation on pure $CuWO_4$, Ag_2MoO_4, 5% MW, 10% MW, and 15% MW photocatalysts

Catalysts	**Rate constant (mol L^{-1} Sec^{-1})**	**R^2**
Pure $CuWO_4$	0.1×10^{-3}	1
Pure Ag_2MoO_4	2.1×10^{-3}	0.902
5% MW	2.5×10^{-2}	0.987
10% MW	0.5×10^{-3}	0.983
15% MW	0.4×10^{-3}	0.997

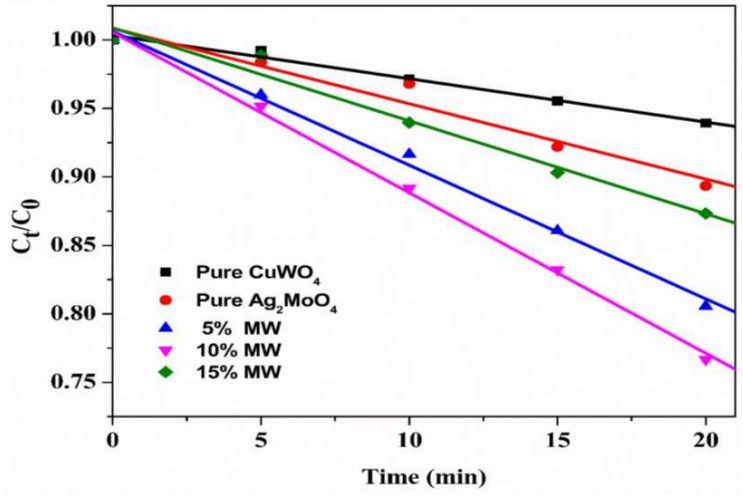

Fig. 6.9: Kinetic plot for RhB degradation with 10% MW photocatalyst

We have additionally estimated turnover frequencies (TOF). The TOF for several photocatalysts from articles that have already been published in the literature is compared in Table 6.2. One of the best values for RhB degradation reported in the literature is the TOF value demonstrated over 10% MW.

Table 6.2: Comparison of MO degradation turnover frequency (TOF) values over different photocatalysts with 10% MW

Photocatalysts	Light source	Turnover frequency ($mol.g^{-1}.min^{-1}$)	References
Ag_2MoO_4/WO_3	300W Xe lamp	0.012×10^{-3}	(Wang et al., 2019)
β-$Ag_2MoO_4/BiVO_4$	300W Xe lamp	4.63×10^{-3}	(Chen et al., 2019)
Ag_3PO_4/Ag_2MoO_4	300W Xe lamp	7.7×10^{-3}	(Cao et al., 2017)
$Ag_2MoO_4/CuWO_4$	250W Hg lamp	3.5×10^{-3}	This work

6.3.7. Recyclability

The recyclability of 10% MW for RhB degradation has been examined under the same experimental conditions for all cycles. The reusability of RhB throughout five cycles is shown in histogram fashion in Fig. 6.10a. A fixed concentration of an aqueous organic pollutant solution was treated to ultraviolet conditions for one hour throughout each cycle. In the following cycle, the photocatalyst was collected and employed again under identical circumstances. According to the results from the first cycle, the degradation indicated in the following cycles was relative. The deterioration rate has dropped to 90% of the output from the first cycle by the fifth cycle. As a result, 10% MW has substantially better photostability than has been observed for pure Ag_2MoO_4. The XRD of the regenerated 10% MW photocatalyst is shown in Fig. 6.10b. Peaks in a fresh powder sample of 10% MW are also observed in reused sample XRD, validating the improved photo-stability of the composite.

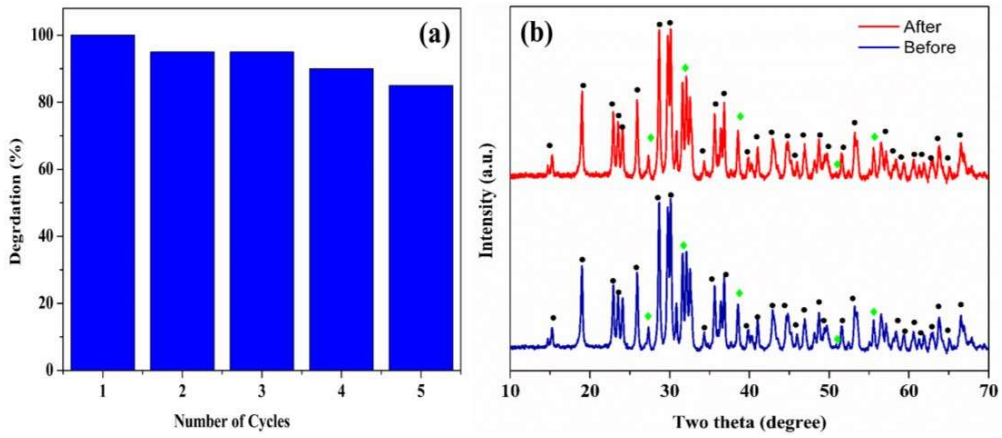

Fig. 6.10: (a) Photocatalytic activity of 10 % MW during five cycles of reuse, (b) XRD of 10% MW before and after 5th catalytic run

6.3.8. Scavenger test

Fig. 6.11 shows a bar plot of the change in RhB degradation when the reaction mixture includes scavengers for trapping active species. The photocatalytic degradation seen over a certain period without any scavenger molecules is represented by the first bar labeled "blank" in the plot. The other bars in the plot are relative to the blank output. Separate photocatalytic tests were carried out with equal amounts of KI, isopropyl alcohol, and p-benzoquinone. The superoxide scavenger PBQ was mainly responsible for RhB degradation. The hole scanger KI also reduced the RhB degradation activity. But the effect was lesser than that seen with PBQ. The hydroxyl radical trapping substance IPA barely impacted the photocatalytic degradation activity. Therefore, superoxide generation and hole oxidation were the fundamental driving forces for photocatalytic degradation. In the last control experiment, acetonitrile was used in place of water as the solvent. Photocatalysis was conducted with continuous oxygen purging. The other photocatalysis parameters stayed the same. RhB showed minimal deterioration in these circumstances.

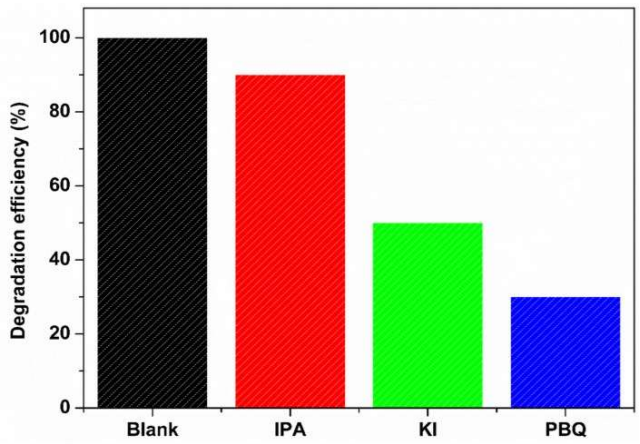

Fig. 6.11: Scavenging experiment histogram plot for determination of the active species during photocatalytic RhB degradation. Blank means photocatalytic degradation (on 10% MW) without any scavenger molecule.

6.3.9. Photocatalytic reaction mechanism

Based on the research findings previously reported, the photocatalytic mechanism is suggested in this section. According to the XPS study, an electron transfer process based on the Z-scheme occurs from the $CuWO_4$ side to the Ag_2MoO_4 portion. Additionally, the results of the scavenger tests show that superoxide and holes are active species that drive photocatalytic activity. Considering these findings, we suggest that 10% MW nanocomposites follow the Z-scheme mechanism. While the holes are localized on the $CuWO_4$ VB, the photoexcited $CuWO_4$ electrons go to Ag_2MoO_4. The superoxide species is created concurrently by reducing oxygen molecules by the photoexcited electrons on Ag_2MoO_4 (Fig. 6.12). Superoxide radical formation justifies the assumption that photo-excited electrons are concentrated on the Ag_2MoO_4 CB. XPS results also demonstrate the migration of charges from $CuWO_4$ to Ag_2MoO_4. The migration of electrons from $CuWO_4$ to Ag_2MoO_4 suppresses electron-hole recombination, increasing photocatalytic efficiency. PL spectra studies also show that electron-hole recombination is lesser in the 10% MW photocatalyst.

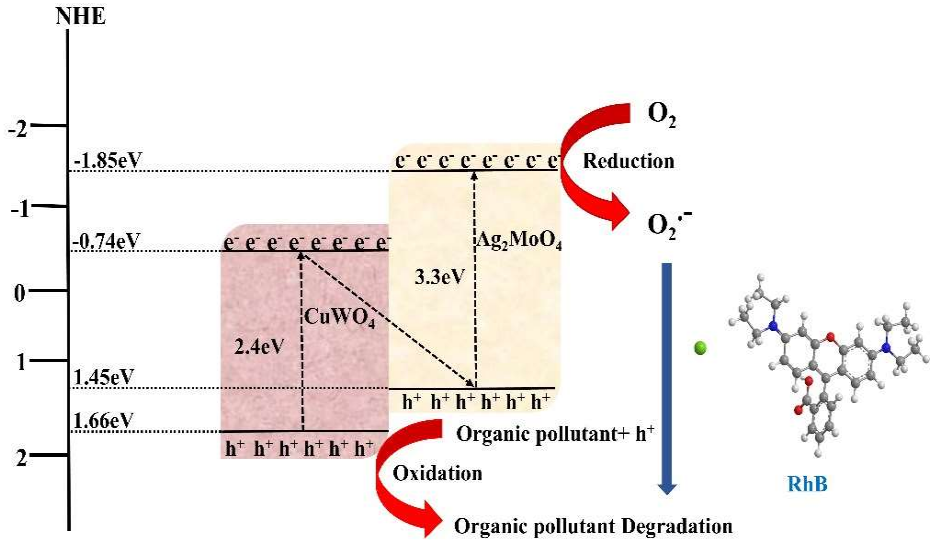

Fig. 6.12: A schematic of the possible photocatalytic mechanism for RhB degradation on 10% MW

6.4. Conclusions

By precipitating varying concentrations of Ag_2MoO_4 (5, 10, and 15 weight percent) on $CuWO_4$ nanoparticles, three $Ag_2MoO_4/CuWO_4$ nanocomposites were prepared and named as 5% MW, 10% MW, and 15% MW. The photocatalytic effectiveness for the degradation of RhB has been found to be efficient in the nanocomposite with a 10 wt% Ag_2MoO_4 loading. The kinetics of photocatalytic degradations follow zero-order kinetics. The electron transfer from the $CuWO_4$ to Ag_2MoO_4 side has been observed in the composite as revealed by XPS examination of the binding energies of the various elements. The scavenger experiment establishes that superoxide radicals are the active ingredient in the photooxidation of RhB.